Analytical Model of Single-Sided Linear Induction Motors for High-Speed Applications

1st Simone Rametti
Distributed Electrical Systems Laboratory (DESL)
Swiss Federal Institute of Technology (EPFL)
Lausanne, Switzerland
simone.rametti@epfl.ch

2nd Lucien Pierrejean
Distributed Electrical Systems Laboratory (DESL)
Swiss Federal Institute of Technology (EPFL)
Lausanne, Switzerland
lucien.pierrejean@epfl.ch

3rd André Hodder
Distributed Electrical Systems Laboratory (DESL)
Swiss Federal Institute of Technology (EPFL)
Lausanne, Switzerland
andre.hodder@epfl.ch

4th Mario Paolone
Distributed Electrical Systems Laboratory (DESL)
Swiss Federal Institute of Technology (EPFL)
Lausanne, Switzerland
mario.paolone@epfl.ch

Abstract—This article describes a field-based analytical model of single-sided linear induction motors (SLIMs) that explicitly considers the following effects altogether: finite motor length, magnetomotive force mmf space harmonics, slot effect, edge effect, and tail effect. The derived closed-form solution of the system's differential equations makes the model computationally more efficient than traditional finite elements (f.e.m.) models, and, therefore, more suitable for SLIM design optimization processes. The computational performance and accuracy of the proposed analytical model are validated through numerical simulations (via COMSOL Multiphysics) and experimental measurements carried out through a dedicated test bench.

Index Terms—Linear induction motor (LIM), magnetic levitation, magnetic vector potential, modeling, transportation

I. INTRODUCTION

THE electrification of transportation, driven by the need to reduce reliance on fossil fuels [1], is emphasized by the increasing number of electric vehicles for low-speed and short-distance travels [2]. For extended distances, the magnetic levitation train represents a promising solution to achieve high commercial speeds (i.e. $v_m \geq 100\,\mathrm{m\,s^{-1}}$), and linear induction motors (LIMs), have been extensively studied during the 20th century as a promising candidate propulsion device for levitated vehicles [3]–[8]. Compared to other linear electric motors, LIMs have several advantages, such as infrastructure passivity (i.e., reaction rails do not need to be magnetized nor electrified), construction simplicity, and simultaneous contact-less thrust and levitation forces generation [6]. Proper mathematical models represent thus fundamental tools for the optimal design of such motors since they allow to derive LIM configurations that maximize certain metrics such as lift and thrust density, efficiency, or a combination of them. However, to the best of the authors' knowledge, the literature lacks accurate and computationally efficient models

of LIMS that are experimentally validated up to high speed (i.e., $v_m \simeq 100\,\mathrm{m\,s^{-1}}$). Within this context, this article proposes a pseudo-three-dimensional field analysis model of short-primary SLIMs where the system's governing differential equations have been analytically solved by imposing proper modeling assumptions. The proposed analytical model explicitly considers the following LIM effects altogether:

1) Finite motor length (extremity effect).
2) Finite motor width (edge effect).
3) Winding harmonics.
4) Slots effect.
5) Effect of the electromagnetic fields at the rear of the motor (hereafter referred to as tail effect).

The proposed model is an extension of the double-sided LIM (DSLIM) analytical model described in [9], with the main differences and contributions listed hereafter:

1) Adaptation of the boundary conditions, geometry, and hypotheses of [9] to comply with the SLIM case study.
2) The DSLIM model proposed in [9] has been improved in this article by integrating the winding AC resistance model and the computation of the SLIM efficiency.
3) In addition to thrust and lift, the efficiency calculation has also been validated through experimental measurements.

The article is structured as follows: Section II describes the proposed SLIM analytical model, from geometry and hypotheses definition to the formulation of the magnetic vector potential differential equations and their solution. Section III presents the numerical and experimental validation of the proposed model through a comparison with f.e.m. simulations and measurements obtained from a custom-made test bench capable of reaching speeds up to $100\,\mathrm{m\,s^{-1}}$. Section IV summarizes the proposed SLIM analytical model and the validation results, and concludes the article.
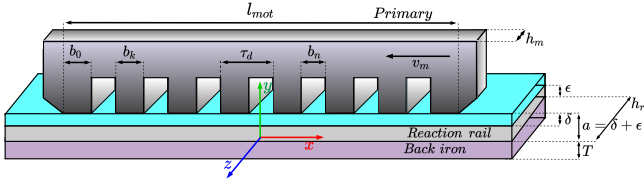
Fig. 1. Realistic SLIM geometry and reference frame.

Fig. 2. Simplified SLIM geometry

II. ANALYTICAL MODEL DESCRIPTION

A. SLIM Model Geometry

Fig. 1 shows the reference frame and the geometry of the SLIM under analysis. As known, short-primary SLIMs are usually made of two main parts [10]:

1) A ferromagnetic moving part with the motor's winding, usually referred to as "Primary".
2) A passive rail installed along the track and composed of a conductive reaction plate of thickness ϵ (e.g., Aluminum) on top of a ferromagnetic plate of thickness T, usually called "back iron".

The space that separates the two parts is called "air gap", and is identified by the symbol δ in Fig. 1. Similarly to [9], the proposed analytical model refers to the simplified geometry represented in Fig. 2, where some hypotheses have been made to simplify the analysis. As can be seen in Fig. 2, the chosen SLIM winding is a three-phase double-layer winding with one slot per pole per phase (i.e., $NSPP = 1$). However, the proposed analytical model is valid for any type of winding. The SLIM direction of movement is along the $\hat{\mathbf{x}}$ axis (negative direction) and the winding conductors are placed along the $\hat{\mathbf{z}}$ axis only, and so is the magnetic vector potential $\vec{A} = A_z(x, y)\hat{\mathbf{z}}$.

B. Problem Statement

In steady state, the magnetic vector potential $A_z(x, y)$ in the SLIM region satisfies the following differential equation [11], [12]:

$$\nabla^2 A_z(x,y) = \mu\sigma \left(j\omega A_z(x,y) + v_m \frac{\partial A_z(x,y)}{\partial x} \right) \quad (1)$$

where $A_z(x, y)$ is the magnetic vector potential $\hat{\mathbf{z}}$ component, v_m is the LIM velocity, μ and σ are the magnetic permeability and conductivity of the considered medium. For the targeted motor geometry, (1) is valid in any domain and is solved in the four different regions represented in Fig. 2 (i.e., Primary, air gap, reaction rail, and back iron). The model's results are expressed in terms of electromagnetic field distributions, efficiency, and longitudinal and transverse forces at different slip operating points.

C. Model Hypotheses

1) Primary dimensions along $\hat{\mathbf{x}}$ and $\hat{\mathbf{y}}$ axis are infinite.
2) The back iron has infinite thickness T, infinite magnetic permeability μ_{fe}, and zero electrical conductivity.
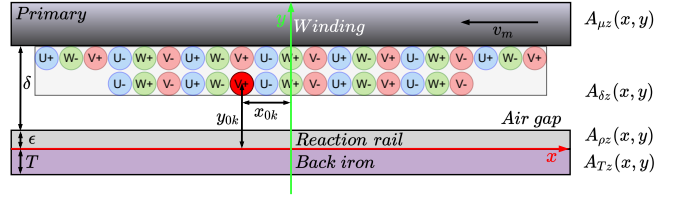3) Air gap δ is uniform, constant, and slot-less throughout the whole domain.

4) The primary winding is represented as a sequence of infinite wires along the $\hat{\mathbf{z}}$ axis distributed in the air gap, as shown in Fig. 2. Each wire carries the current $n_{wk}\overline{I}_{0k}$ (current expressed in RMS value), where n_{wk} is the number of turns in the kth conductor.
5) The reaction rail is homogeneous with constant relative permeability $\mu_r = 1$, permittivity ϵ_{Al}, electrical conductivity σ, and thickness ϵ.
6) The primary has infinite magnetic permeability μ_{fe} and zero electrical conductivity. As a consequence, iron saturation is neglected and the superposition principle can be applied[1].
7) The study is performed in steady-state conditions (i.e. in the frequency domain, with phasors).

D. Source Magnetic Vector Potential

With reference to Fig. 2, hypotheses 4, 6, 7, and inspired by [9], [12], the input source of the model is represented by the algebraic sum of the magnetic vector potentials generated by each conductor in the air gap, in the absence of the primary, reaction rail and back iron. It is directly derived from the Biot-Savart law [15]:

$$A_z^s(x,y) = \sum_k \frac{-n_{wk}\overline{I}_{0k}\mu_0}{2\sqrt{2}\pi} \ln\left(\frac{(x - x_{0k})^2 + (y - y_{0k})^2}{R_{0k}^2} \right) \quad (2)$$

where the coordinates of the kth conductor's center, of radius R_{0k}, are expressed by x_{0k} and y_{0k}. Since the system is linear, as stated in Hypothesis 6, the solution of (1) in the air gap is written as the sum of the source magnetic vector potential $A_z^s(x, y)$ and the result of the interaction between the SLIM primary and the reaction rail plus back iron.

E. Solution of the Magnetic Vector Potential

The general solution of (1) is derived through a complex Fourier series decomposition in the interval $x \in [-L/2, L/2]$, where L is the period of the Fourier series. Similarly to [9], [12], [16], [17], it has the following form:

$$A_z(x,y) = \sum_{n=-\infty}^{\infty} e^{j\lambda_n x} \left(\beta_n e^{\gamma_n y} + \Gamma_n e^{-\gamma_n y} \right) \quad (3)$$

where $\lambda_n = \frac{2\pi n}{L}$, $\gamma_n = \sqrt{\lambda_n^2 + j\mu\sigma(\omega + v_m\lambda_n)}$, and $\omega = 2\pi f_s$, with f_s being the supply frequency.

---

[1]The hypothesis is justified assuming that the iron core is designed such that the intensity of the magnetic flux density at null speed is below the saturation level of the considered ferromagnetic material (e.g. between $1.5\,\text{T}$ and $2.4\,\text{T}$ as shown in [13], [14]). At high speed, the intensity of the magnetic flux density decreases.

Some simplifications are applied to (3) based on the region where the solution is considered:

1) Primary: according to Hypothesis 6, the electrical conductivity is zero, and hence: $\gamma_n = |\lambda_n|$. Moreover, for $y \to \infty$, $A_{\mu z}(x, y) \to 0$, and thus the integration constant β_n has to be 0.
2) Air gap: electrical conductivity is zero, hence: $\gamma_n = |\lambda_n|$. Moreover, as mentioned above, the source magnetic vector potential $A_z^s(x, y)$ has to be added to (3).
3) Reaction rail: the general formulation of (3) is used.
4) Back iron: according to Hypothesis 2, the electrical conductivity is zero, and hence: $\gamma_n = |\lambda_n|$. Moreover, for $y \to -\infty$, $A_{Tz}(x, y) \to 0$, and thus the integration constant Γ_n has to be 0.

By applying the above-mentioned simplifications to the general formulation of (3), the solution of (1) in the four regions of interest becomes the following:

$$
\begin{cases}
A_{\mu z}(x, y) = \sum_n e^{j\lambda_n x} \Gamma_{\mu n} e^{-|\lambda_n| y} \\
A_{\delta z}(x, y) = A_z^s(x, y) + \sum_n e^{j\lambda_n x} \left(\beta_{\delta n} e^{|\lambda_n| y} + \Gamma_{\delta n} e^{-|\lambda_n| y} \right) \\
A_{\rho z}(x, y) = \sum_n e^{j\lambda_n x} \left(\beta_{\rho n} e^{\gamma_n y} + \Gamma_{\rho n} e^{-\gamma_n y} \right) \\
A_{Tz}(x, y) = \sum_n e^{j\lambda_n x} \beta_{Tn} e^{|\lambda_n| y}
\end{cases}
\tag{4}
$$

The six integration constants are determined by imposing six boundary conditions at the various interfaces between materials, as described hereafter.

F. Boundary Conditions Formulation

The following Neumann boundary conditions are applied at the interface between two media [18]:

1) Continuity of the magnetic flux density normal component $\hat{r} \cdot \left(\vec{B}_1 - \vec{B}_2 \right)$.
2) Continuity of the magnetic field tangential component $\hat{r} \times \left(\vec{H}_1 - \vec{H}_2 \right)$.

Where $\hat{r}$ is the versor perpendicular to the considered surface. The above boundary conditions are applied at each material interface of the SLIM geometry of Fig. 2. The solution is the same as the one of the DSLIM model described in [9], with the substitution $\epsilon/2 \to \epsilon$, since in a SLIM no symmetry is applied in the middle of the reaction rail (contrary to a DSLIM).

G. Electromagnetic Fields Calculation

Once the magnetic vector potential solution is derived, the electromagnetic fields can be calculated by recalling the definition of the magnetic vector potential and Faraday's law:

$$
\vec{B} = \nabla \times \vec{A} \qquad \vec{E} = -\frac{\partial \vec{A}}{\partial t} \tag{5}
$$

By applying (5) to (4) the distributions of the magnetic flux density and the electric field are obtained. Of particular interest

are the distributions in the air gap and reaction rail, which are reported hereafter.

$$
\begin{cases}
B_{\delta y}(x, y) = B_y^s(x, y) - j \sum_n \lambda_n e^{j\lambda_n x} \left(\beta_{\delta n} e^{|\lambda_n| y} + \Gamma_{\delta n} e^{-|\lambda_n| y} \right) \\
B_{\delta x}(x, y) = B_x^s(x, y) + \sum_n |\lambda_n| e^{j\lambda_n x} \left(\beta_{\delta n} e^{|\lambda_n| y} - \Gamma_{\delta n} e^{-|\lambda_n| y} \right) \\
B_{\rho y}(x, y) = -2j \sum_n \lambda_n e^{j\lambda_n x} \beta_{\rho n} \cosh(\gamma_n y) \\
B_{\rho x}(x, y) = 2 \sum_n \gamma_n e^{j\lambda_n x} \beta_{\rho n} \sinh(\gamma_n y)
\end{cases}
\tag{6}
$$

$$
\begin{cases}
E_{\delta z}(x, y) = -j\omega A_z^s(x, y) - j\omega \sum_n e^{j\lambda_n x} \left(\beta_{\delta n} e^{|\lambda_n| y} + \Gamma_{\delta n} e^{-|\lambda_n| y} \right) \\
E_{\rho z}(x, y) = -2j\omega \sum_n e^{j\lambda_n x} \beta_{\rho n} \cosh(\gamma_n y)
\end{cases}
\tag{7}
$$

The hyperbolic functions in (6) and (7) are introduced as a consequence of the boundary conditions, where it can be shown that $\beta_{\rho n} = \Gamma_{\rho n}$ (see [9] for further details).

H. SLIM Forces Calculation

The forces applied by the SLIM primary to the reaction rail are calculated through the integration of Maxwell's stress tensor along the rail surface:

1) Longitudinal force (thrust) along the $\hat{x}$ axis, F_x.
2) Transverse (or normal) force along the $\hat{y}$ axis, F_y.

Hence:

$$
F_x = -\frac{h_m}{2\mu_0} \int_{-L/2}^{L/2} \Re \left(B_{\rho x}^* \left(x, \frac{\epsilon}{2} \right) B_{\rho y} \left(x, \frac{\epsilon}{2} \right) \right) \, dx \tag{8}
$$

$$
F_y = \frac{h_m}{4\mu_0} \int_{-L/2}^{L/2} \left(\left| B_{\rho y} \left(x, \frac{\epsilon}{2} \right) \right|^2 - \left| B_{\rho x} \left(x, \frac{\epsilon}{2} \right) \right|^2 \right) \, dx \tag{9}
$$

where h_m is the primary width along the $\hat{z}$ axis, the $*$ denotes the complex conjugate, and a factor $\frac{1}{2}$ has to be added to transform the forces from peak to RMS values. By substituting (6) into (8) and (9) one obtains the final formulation of the SLIM electromagnetic forces:

$$
F_x = -2\Phi \sum_n \Re \left[\left(\beta_{\rho n} \gamma_n \sinh(\vartheta_n) \right)^* \left(-j\lambda_n \beta_{\rho n} \cosh(\vartheta_n) \right) \right] \tag{10}
$$

$$
F_y = \Phi \sum_n \left(\left| \lambda_n \beta_{\rho n} \cosh(\vartheta_n) \right|^2 - \left| \gamma_n \beta_{\rho n} \sinh(\vartheta_n) \right|^2 \right) \tag{11}
$$

where $\Phi = \left(Lh_m / \mu_0 \right)$, and $\vartheta_n = \gamma_n \epsilon$.

I. Primary-to-Rail Complex Power

The electromagnetic power transmitted from the primary to the reaction rail is computed through the integral of the Poynitng vector evaluated at the rail surface (i.e., $y = \epsilon$)[2]:

$$
P_\rho = \frac{h_m}{2} \int_{-L/2}^{L/2} \vec{E}_\rho \times \vec{H}_\rho^* \, dx = \frac{h_m}{2} \int_{-L/2}^{L/2} E_{\rho z}(x, \epsilon) \cdot H_{\rho x}^*(x, \epsilon) \, dx \tag{12}
$$

---

[2]The rail surface has been chosen for the evaluation of P_ρ to capture the mechanical power transmitted to rail plus the Joule losses dissipated in it.
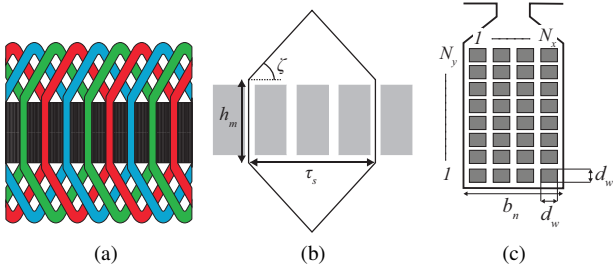
Fig. 3. Double-layer distributed winding pattern (a), coil geometry (b), and slot detail (c) for the SLIM of Table I

By substituting (6) and (7) into (12) and after some simplifications, one obtains the following expression for the Poynitng vector:

$$P_\rho = -2j\omega\Phi \sum_n \beta_{\rho n} \cosh(\vartheta_n) \left(\gamma_n \beta_{\rho n} \sinh(\vartheta_n)\right)^* \tag{13}$$

J. SLIM Efficiency Calculation

According to Hypotheses 2 and 6, core and back iron losses have been neglected. Therefore, the SLIM efficiency may be computed as follows:

$$\eta = \frac{v_m F_x}{\Re\{P_\rho\} + P_{js}} \tag{14}$$

where P_{js} are the Joule losses due to the windings $P_{js} = 3R_{ph}I^2$, and R_{ph} is the winding AC phase resistance. For the double-layer distributed winding shown in Fig. 3a, R_{ph} can be calculated as follows:

$$R_{ph} = K_s R_{DC} = K_s \left(2p\ NSPP\ \frac{\rho_w N l_w}{N_p S_w}\right) \tag{15}$$

where R_{DC} is the winding DC resistance, K_s is the skin effect resistance factor, p is the number of pole pairs, ρ_w the resistivity of the conductor, N the number of turns per coil, S_w the wire cross-section, N_p the number of conductors in parallel, and l_w the average length of a coil turn, approximated by:

$$l_w = 2(h_m + \frac{\tau_s}{\cos\zeta}) \tag{16}$$

where τ_s is the coil span, and ζ is the angle between the end winding and the primary, as illustrated in Fig. 3b. The skin effect resistance factor K_s has been derived from [14] for the case of a slot filled with rectangular conductors of side d_w, as shown in Fig. 3c.

$$K_s = \xi \frac{\sinh(2\xi) + \sin(2\xi)}{\cosh(2\xi) - \cos(2\xi)} + \frac{2\xi\left(N_y^2 - 1\right)(\sinh(\xi) - \sin(\xi))}{3(\cosh(\xi) + \cos(\xi))} \tag{17}$$

And:

$$\xi = d_w \sqrt{\frac{1}{2\rho_w}\omega\mu_0 \frac{N_x d_w}{b_n}} \tag{18}$$

where b_n is the slot width.

K. Hypotheses Compensation

The simplifications introduced by some of the hypotheses have been compensated in the same way described in [9]. For the sake of clarity, they are summarized hereafter.

1) Slot-Less Air Gap Compensation: Hypothesis 3 states that the air gap is uniform throughout the Fourier series period and does not have slots. To compensate for the assumption, a correction of the air gap through Carter's coefficient is done [6], [19]. With reference to [14], [20], the equivalent slotted air gap δ_e is derived as:

$$\delta_e = \frac{\tau_p}{\tau_p - kb_n}\delta \tag{19}$$

where τ_p is the LIM pole pitch. The coefficient k is derived from [14]:

$$k = \frac{2}{\pi}\left[\arctan\left(\frac{b_n}{2\delta}\right) - \frac{2\delta}{b_n}\ln\sqrt{1 + \left(\frac{b_n}{2\delta}\right)^2}\right] \tag{20}$$

2) Edge Effect Compensation: The proposed analytical model is bi-dimensional. However, a correction of the reaction rail electrical conductivity, reflecting the motor's finite width (i.e., the edge effect), is derived through the Russel-Norsworthy coefficient [21].

$$K_\rho = 1 - \frac{\tanh(\chi)}{\chi\left(1 + \tanh(\chi)\tanh\left(\frac{\pi}{\tau_p}\left(\frac{h_r - h_m}{2}\right)\right)\right)} \tag{21}$$

where h_r is the reaction rail width along the $\hat{\mathbf{z}}$ axis, and $\chi = (\pi h_m)/(2\tau_p)$. Hence, the equivalent reaction rail electrical conductivity σ_e can be calculated as:

$$\sigma_e = K_\rho \sigma \tag{22}$$

3) Uniform and Constant Air Gap Compensation: Hypotheses 1 and 3 state that the SLIM air gap is constant and uniform throughout the whole Fourier series period. This effect has been called the "tail effect" and leads to an overestimation of the forces developed by the SLIM. To compensate for this effect, the forces developed by the rear section of the LIM only (i.e., tail) are computed by evaluating the integrals (8) and (9) in the interval $x \in [l_{mot}/2, L/2]$, where l_{mot} is the length of the primary. Thanks to the linearity of the model, the obtained forces are then subtracted from the thrust and lift calculated through (10) and (11).

III. MODEL VALIDATION

The validity and accuracy of the proposed SLIM analytical model have been assessed through both f.e.m. simulations and measurements obtained from a dedicated test bench. The SLIM used in the validation is half of the double-sided LIM used in [9], and its geometry is reported in Table I.

A. SLIM Test Bench

The test bench used in [9] to experimentally validate the DSLIM has been assembled in a SLIM configuration. In this respect, the 2 mm-thick AW-5005 aluminum rail is joined with a 3 mm-thick DC01 back iron. Fig. 4 shows the test bench.

B. F.e.m. Model

To numerically validate the proposed SLIM analytical model, a 2D f.e.m. model has been built in COMSOL Multiphysics through the magnetic field (mf) interface of the AC/DC module [22]. Details of the COMSOL model are reported in [9].
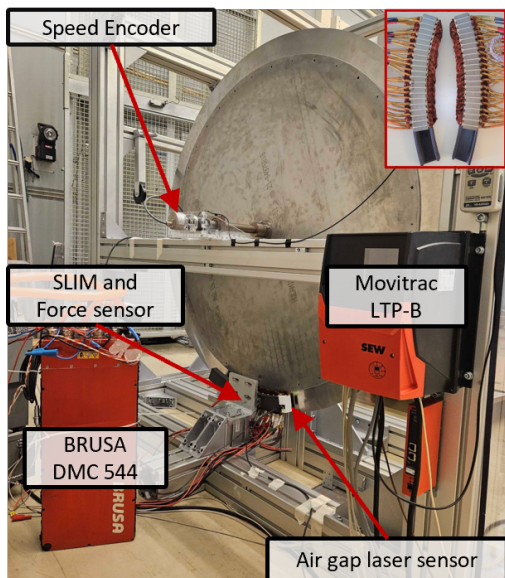
Fig. 4. Picture of the SLIM test bench

TABLE I
SLIM REFERENCE GEOMETRY.

Parameter	Symbol	Value
Pole pitch	τ_p	$0.045\,\mathrm{m}$
Number of pole pairs	p	3
Number of phases	m	3
Rail thickness	ϵ	$2\,\mathrm{mm}$
Nominal air gap	δ_n	$5\,\mathrm{mm}$
Number of slot/pole/phase	$NSPP$	1
Number of turns per coil	N	15
Number of conductors in parallel	N_p	2
Number of conductors along the $\hat{\mathbf{x}}$ axis	N_x	4
Number of conductors along the $\hat{\mathbf{y}}$ axis	N_y	8
Conductor diameter	d_w	$1.12\,\mathrm{mm}$
Supply nominal current	I	$15\,\mathrm{Arms}$
Motor width	h_m	$0.04\,\mathrm{m}$
Slot width	b_n	$8\,\mathrm{mm}$
Motor length	l_{mot}	$35\,\mathrm{cm}$

C. Key Performance Indicators

The comparison between the proposed model, the COMSOL f.e.m. model, and the experimental measurements is performed by comparing thrust and lift forces at different operating points. The same KPIs as [9] are used. They are reported hereafter for the sake of clarity:

- Maximum error to capture the highest difference between the forces computed by the proposed LIM model vs the f.e.m. benchmark.
- RMS error to quantify the average quality of the forces computed by the proposed LIM model vs the f.e.m. benchmark.

D. Numerical Validation Via COMSOL

The thrust and lift comparisons between the proposed SLIM analytical model and the f.e.m. are shown in Fig. 5, whereas Fig. 7 shows the maximum and RMS errors for each simulated

characteristic. As can be noticed, the proposed analytical model exhibits excellent accuracy and one can further notice the following:

- Both Maximum and RMS errors are bounded in each simulation.
- RMSE, which represents the most relevant metric to assess the model's accuracy, is bounded to less than $3\,\%$ and $1\,\%$ for lift and thrust respectively.
- The maximum error is bounded to $4.5\,\%$ and $2\,\%$ for lift and thrust respectively.

Furthermore, the greatest advantage of the proposed analytical model is its higher computation efficiency compared to f.e.m. models, as reported in Table II, which makes the model suitable to be coupled with optimization frameworks for the design phase of SLIMs, whereas, an f.e.m.-based optimization would take too much time and thus be impractical.

E. Experimental Validation

The comparisons between simulated and measured thrust and lift are shown in Fig. 6, whereas Fig. 8 shows the comparison between the simulated and measured efficiency. The shaded areas in Fig. 6 represent the air gap interval, centered around the nominal value, that has been used in the simulations to account for the air gap variations due to the test bench disk irregularities (i.e., $\delta = \delta_n \pm 0.5\,\mathrm{mm}$) [9]. As can be noticed, the proposed analytical model exhibits excellent accuracy compared to the experimental data. It is worth noticing that, as expected, the simulated efficiency is overestimated due to the absence of core and back iron losses in the analytical model, with the RMSE bounded to $3.3\,\%$.

TABLE II
COMPARISON OF THE COMPUTATION TIMES FOR A DIFFERENT NUMBER OF SUPPLY FREQUENCIES.

Simulation type	Analytical	COMSOL
Single supply frequency	$\simeq 3.5\,\mathrm{s}$	$\simeq 0.5\,\mathrm{h}$
Full characteristic (15 frequencies)	$\simeq 25\,\mathrm{s}$	$\simeq 3\,\mathrm{h}$

IV. CONCLUSIONS

The article proposes a quasi-three-dimensional model of a SLIM, obtained through a Fourier series decomposition method, whose derivation has been described in detail. The model's results have been validated through both numerical simulations, obtained through COMSOL f.e.m. models, and experimental results, obtained with a dedicated test bench. The proposed model explicitly takes into account the main characteristics of SLIMs, it is computationally efficient and very accurate up to high speed (i.e, $v_m \simeq 100\,\mathrm{m\,s^{-1}}$). The comparison of simulated thrust and lift with COMSOL f.e.m. models has shown that maximum and RMS errors are always bounded and that RMS error is below $3\,\%$ and $1\,\%$ for lift and thrust respectively. Moreover, the experimental results confirmed the accuracy of the proposed model throughout the whole speed range of interest. The efficiency calculation,
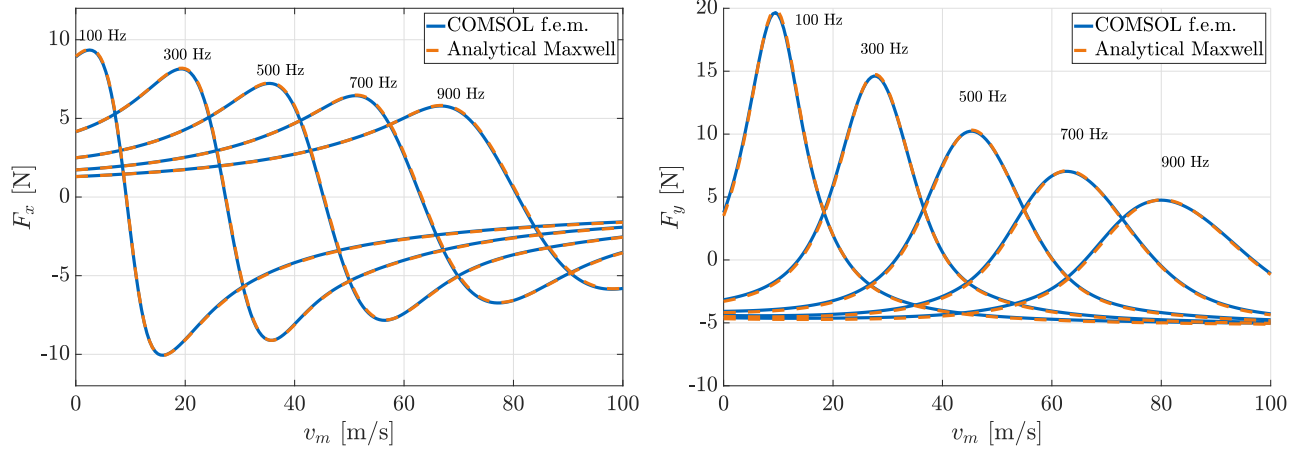
Fig. 5. Longitudinal force F_x and normal force F_y comparisons between analytical model and COMSOL f.e.m. simulations.
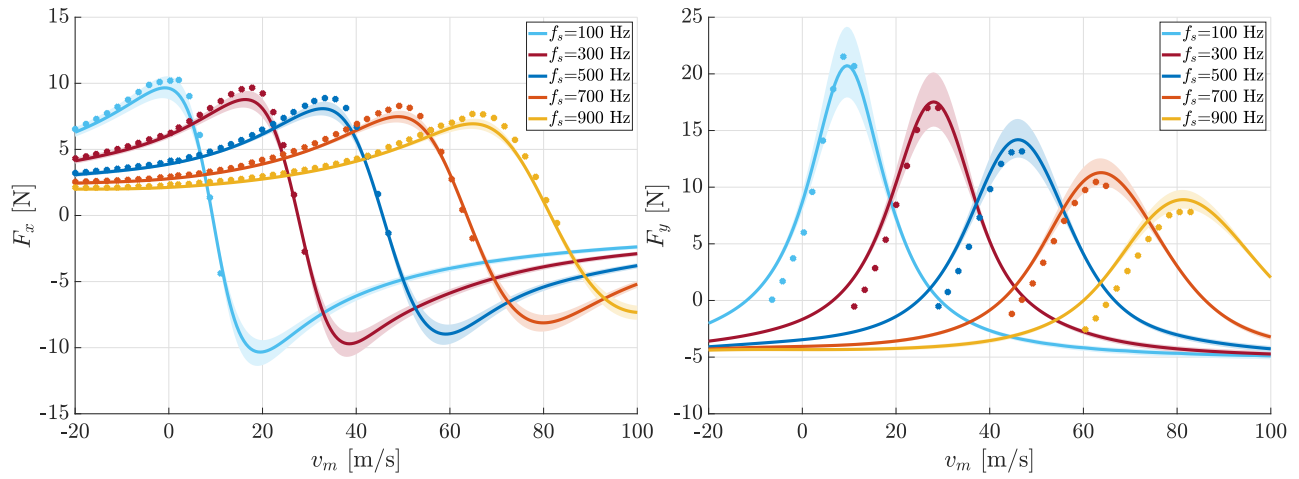

Fig. 6. Longitudinal force F_x and normal force F_y comparisons between measurements (dots) and the proposed analytical model (solid) with $\delta_n = 5\,\mathrm{mm}$. The shaded areas represent the air gap interval used in the simulations.
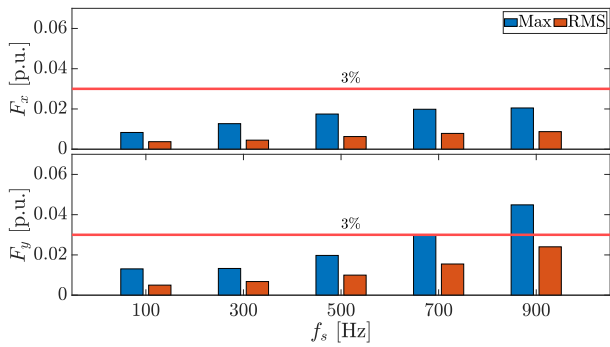

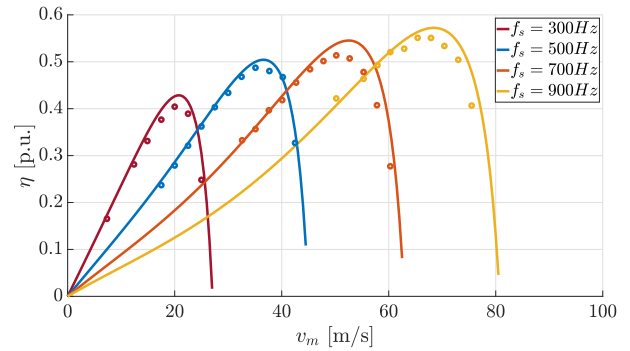Fig. 7. Maximum and RMS errors between the analytical model and COMSOL f.e.m. simulations.

Fig. 8. Efficiency comparison between measurements (dots) and the proposed analytical model (solid).

although overestimated due to the absence of core and back iron losses in the model, proves to be very accurate in comparison with the measurements, with the RMSE bounded to 3.3 %. Finally, the high computation efficiency, compared to f.e.m. models, is the greatest advantage of the proposed model,

which makes it possible to be integrated into design-oriented optimization processes.

REFERENCES

[1] IEA, "Energy consumption in transport by fuel in the Net Zero Scenario, 1975-2030," 2022. [Online]. Available: https://www.iea.org/

data-and-statistics/charts

[2] International Energy Agency, *Global EV Outlook 2023: Catching up with Climate Ambitions*, ser. Global EV Outlook. OECD, Apr. 2023. [Online]. Available: https://www.oecd-ilibrary.org/energy/global-ev-outlook-2023_cbe724e8-en

[3] E. Laithwaite and F. Barwell, "Linear induction motors for high-speed railways," *Electronics and Power*, vol. 10, no. 4, pp. 100–103, Apr. 1964.

[4] R. Hellinger and P. Mnich, "Linear Motor-Powered Transportation: History, Present Status, and Future Outlook," *Proceedings of the IEEE*, vol. 97, no. 11, pp. 1892–1900, Nov. 2009.

[5] T. C. Wang, "Linear Induction Motor for High-Speed Ground Transportation," *IEEE Transactions on Industry and General Applications*, vol. IGA-7, no. 5, pp. 632–642, Sep. 1971.

[6] S. E. Abdollahi, M. Mirzayee, and M. Mirsalim, "Design and Analysis of a Double-Sided Linear Induction Motor for Transportation," *IEEE Transactions on Magnetics*, vol. 51, no. 7, pp. 1–7, Jul. 2015.

[7] T. Higuchi, S. Nonaka, and M. Ando, "On the design of high-efficiency linear induction motors for linear metro," *Electrical Engineering in Japan*, vol. 137, no. 2, pp. 36–43, 2001. [Online]. Available: https://onlinelibrary.wiley.com/doi/abs/10.1002/eej.1086

[8] R. Palka and K. Woronowicz, "Linear Induction Motors in Transportation Systems," *Energies*, vol. 14, no. 9, p. 2549, Jan. 2021. [Online]. Available: https://www.mdpi.com/1996-1073/14/9/2549

[9] S. Rametti, L. Pierrejean, A. Hodder, and M. Paolone, "Pseudo-Three-Dimensional Analytical Model of Linear Induction Motors for High-Speed Applications," *IEEE Transactions on Transportation Electrification*, pp. 1–1, 2024. [Online]. Available: https://ieeexplore.ieee.org/document/10378729/

[10] S. Chevailler, Ed., *Comparative study and selection criteria of linear motors*. Lausanne: EPFL, 2006.

[11] S. Yamamura and H. Ito, "Three-dimensional analysis of linear induction motors," *Electrical Engineering in Japan*, vol. 96, no. 2, pp. 55–61, 1976. [Online]. Available: https://onlinelibrary.wiley.com/doi/10.1002/eej.4390960208

[12] M. Abdelqader, J. Morelli, R. Palka, and K. Woronowicz, "2-D quasi-static solution of a coil in relative motion to a conducting plate," *COMPEL - The international journal for computation and mathematics in electrical and electronic engineering*, vol. 36, no. 4, pp. 980–990, Jan. 2017. [Online]. Available: https://doi.org/10.1108/COMPEL-07-2016-0312

[13] M. A. Prabhu, J. Y. Loh, S. C. Joshi, V. Viswanathan, S. Ramakrishna, C. J. Gajanayake, and A. K. Gupta, "Magnetic Loading of Soft Magnetic Material Selection Implications for Embedded Machines in More Electric Engines," *IEEE Transactions on Magnetics*, vol. 52, no. 5, pp. 1–6, May 2016. [Online]. Available: https://ieeexplore.ieee.org/document/7378501/

[14] J. Pyrhonen, T. Jokinen, and V. Hrabovcová, *Design of rotating electrical machines*. Chichester, West Sussex, United Kingdom ; Hoboken, NJ: Wiley, 2008.

[15] T. Charitat and F. Graner, "About the magnetic field of a finite wire," *European Journal of Physics*, vol. 24, no. 3, p. 267, Mar. 2003. [Online]. Available: https://dx.doi.org/10.1088/0143-0807/24/3/306

[16] M. Abdelqader, J. Morelli, R. Palka, and K. Woronowicz, "2-D quasi-static fourier series solution for a single coil of a linear induction motor," in *2016 IEEE Conference on Electromagnetic Field Computation (CEFC)*, Nov. 2016, pp. 1–1.

[17] K. Woronowicz, M. Abdelqader, R. Palka, and J. Morelli, "2-D quasi-static Fourier series solution for a linear induction motor," *COMPEL - The international journal for computation and mathematics in electrical and electronic engineering*, vol. 37, no. 3, pp. 1099–1109, Jan. 2018. [Online]. Available: https://doi.org/10.1108/COMPEL-06-2017-0247

[18] J.-M. Jin, *The finite element method in electromagnetics*, 3rd ed. Hoboken. New Jersey: John Wiley & Sons Inc, 2014.

[19] F. Carter, "The magnetic field of the dynamo-electric machine," *Journal of the Institution of Electrical Engineers*, vol. 64, no. 359, pp. 1115–1138, Nov. 1926. [Online]. Available: https://digital-library.theiet.org/content/journals/10.1049/jiee-1.1926.0122

[20] I. Boldea, *Linear Electric Machines, Drives, and MAGLEVs Handbook*, 1st ed. CRC Press, Dec. 2017. [Online]. Available: https://www.taylorfrancis.com/books/9781439845158

[21] R. L. Russell and K. H. Norsworthy, "Eddy currents and wall losses in screened-rotor induction motors," *Proceedings of the IEE - Part A: Power Engineering*, vol. 105, no. 20, pp. 163–175, Apr. 1958. [Online]. Available: https://digital-library.theiet.org/content/journals/10.1049/pi-a.1958.0036

[22] J.-M. Jin, "Chapter 4: Two-Dimensional Finite Element Analysis," in *The finite element method in electromagnetics*, 3rd ed. Hoboken. New Jersey: John Wiley & Sons Inc, 2014.

Simone Rametti (Graduate Student Member, IEEE) received the B.Sc. degree in electrical engineering from Politecnico di Milano, Milan, Italy, in 2017, and the M.Sc. degree in electrical engineering from the Swiss Federal Institute of Technology (EPFL), Lausanne, Switzerland, in 2019, with specialization in smart grids and renewable applications, where he is currently pursuing the Ph.D. degree with the Distributed Electrical Systems Laboratory. His research interests include modeling linear motors for high-speed transportation systems, magnetic levitation, and energy storage systems.

Lucien Pierrejean received the B.Sc. and M.Sc. degrees in electrical engineering from the Swiss Federal Institute of Technology, Lausanne, Switzerland, in 2020 and 2023, respectively, where he is currently pursuing the Ph.D. degree with the Distributed Electrical Systems Laboratory. His research interests include the electromagnetic modeling of linear motors for the propulsion of high-speed transportation systems.

André Hodder (Senior Member, IEEE) received the degree in electrical engineering and the Doctoral degree from the École Polytechnique Fédérale de Lausanne (EPFL), Lausanne, Switzerland, in 1999 and 2004, respectively. Since 2005, he has been a Lecturer and a Scientific Collaborator at EPFL in the field of electrical machines, energy conversion, and embedded motor control. His recent research activities focus on the design of linear induction motors, homopolar motors, and more generally the propulsion of hyperloop applications.

Mario Paolone (Fellow, IEEE) received the M.Sc. (Hons.) and Ph.D. degrees in electrical engineering from the University of Bologna, Bologna, Italy, in 1998 and 2002, respectively. In 2005, he was an Assistant Professor in power systems with the University of Bologna, where he was with the Power Systems Laboratory until 2011. Since 2011, he has been with the Swiss Federal Institute of Technology, Lausanne, Switzerland, where he is currently a Full Professor and the Chair of the Distributed Electrical Systems Laboratory. His research interests focus on power systems with particular reference to real-time monitoring and operational aspects, power systems protection, dynamics, and transients. His most significant contributions are in the field of PMU-based situational awareness of active distribution networks (ADNs) and in the field of exact, convex, and computationally efficient methods for the optimal planning and operation of ADNs. Dr. Paolone was the Founder and the Editor-in-Chief of Sustainable Energy, Grids and Networks (Elsevier).